





















RESEARCH ARTICLE | DECEMBER 26 2024

Design and commissioning of the PRIOR-II “proton microscope for FAIR”

M. Schanz ; D. Varentsov ; J. C. Allison ; V. Bagnoud ; R. Belikov ; A. Blazevic ;
U. Eisenbarth ; M. S. Freeman ; R. Gavrilin; J. Jacoby; A. G. Kalimov ; A. Khurchiev ;
F. G. Mariam ; F. E. Merrill ; A. Müller-Münster; L. P. Neukirch ; S. Neff ; D. Nikolaev ;
J. L. Schmidt ; A. Skobliakov ; K. Weyrich ; B. Winkler ; B. Zielbauer 



Rev. Sci. Instrum. 95, 123704 (2024)

<https://doi.org/10.1063/5.0220086>



Articles You May Be Interested In

Commissioning of the PRIOR proton microscope

Rev. Sci. Instrum. (February 2016)

PROTON MICROSCOPY AT FAIR

AIP Conference Proceedings (December 2009)

High-energy-density-science capabilities at the Facility for Antiproton and Ion Research

Phys. Plasmas (April 2020)



Special Topics Open for Submissions

[Learn More](#)

Design and commissioning of the PRIOR-II “proton microscope for FAIR”

Cite as: Rev. Sci. Instrum. 95, 123704 (2024); doi: 10.1063/5.0220086

Submitted: 22 May 2024 • Accepted: 4 December 2024 •

Published Online: 26 December 2024



View Online



Export Citation



CrossMark

M. Schanz,^{1,a)} D. Varentsov,¹ J. C. Allison,² V. Bagnoud,¹ R. Belikov,³ A. Blazevic,¹
U. Eisenbarth,¹ M. S. Freeman,² R. Gavrilin,⁴ J. Jacoby,⁵ A. G. Kalimov,⁶ A. Khurchiev,⁴
F. G. Mariam,² F. E. Merrill,² A. Müller-Münster,⁵ L. P. Neukirch,² S. Neff,⁷ D. Nikolaev,⁸
J. L. Schmidt,² A. Skobliakov,⁴ K. Weyrich,¹ B. Winkler,³ and B. Zielbauer¹

AFFILIATIONS

¹Plasmaphysics Department, GSI Helmholtzzentrum für Schwerionenforschung GmbH, Planckstrasse 1, 64291 Darmstadt, Germany

²P-1 Proton Radiography, Los Alamos National Laboratory, Bikini Atoll Rd., TA-53, Los Alamos, New Mexico 87545, USA

³AG Kristallographie/Mineralogie, Institut für Geowissenschaften, Goethe-Universität Frankfurt, Altenhöferallee 1, 60438 Frankfurt am Main, Germany

⁴Laboratory for High Energy Density in Matter Bolshaya, National Research Centre “Kurchatov Institute” - ITP, Cheremushkinskaya 25, 117218 Moscow, Russia

⁵Institute für Angewandte Physik, Plasmaphysik, Goethe-Universität Frankfurt, Altenhöferallee 1, 60438 Frankfurt am Main, Germany

⁶Department of Theoretical Electrical Engineering and Electromechanics, Peter the Great St. Petersburg Polytechnic University, Polytechnicheskaya 29, St. Petersburg 195251, Russia

⁷Facility for Antiproton and Ion Research in Europe GmbH (FAIR), FAIR Research Division, Planckstrasse 1, 64291 Darmstadt, Germany

⁸Federal Research Center of Problems of Chemical Physics and Medicinal Chemistry RAS, High Dynamic Pressure Laboratory Academician, Semenov avenue 1, Chernogolovka 142432, Russia

^{a)}Author to whom correspondence should be addressed: m.schanz@gsi.de

ABSTRACT

A new high energy proton radiography facility PRIOR-II (Proton Microscope for FAIR) has been designed, constructed, and successfully commissioned at the GSI Helmholtzzentrum für Schwerionenforschung (Darmstadt, Germany) pushing the technical boundaries of charged particle radiography with normal conducting magnets to the limits. The setup is foreseen to become a new and powerful user facility for carrying out fundamental science experiments in the fields of plasma and shock wave physics, material science, and medical physics. It will help address several unsolved scientific challenges, which require high-speed and precise non-invasive diagnostic methods capable of probing matter with up to 100 g/cm² areal density. PRIOR-II is specifically designed to utilize the full timing capabilities of the SIS-18 synchrotron at GSI for ultra-fast dynamic experiments with up to 4 GeV protons and will also be fielded at the future FAIR facility, where higher proton energies and beam intensities will be available. This will enable experiment geometries with even higher areal densities, more flexible experiment timing, and further enhanced spatial resolution.

© 2024 Author(s). All article content, except where otherwise noted, is licensed under a Creative Commons Attribution (CC BY) license (<https://creativecommons.org/licenses/by/4.0/>). <https://doi.org/10.1063/5.0220086>

I. INTRODUCTION

Lens-based proton radiography is a powerful technique for probing the interior of dense objects in static or dynamic experiments by mono-energetic beams of GeV-energy protons, using a system of magnetic lenses for imaging.¹

The concept of proton radiography employing magnetic lenses has been developed and demonstrated in the 1990s at the Los Alamos National Laboratory using 800 MeV H^- beams from the LANSCE linear accelerator facility.^{2,3} Since then, several proton radiography facilities using high energy protons from 800 MeV up to 70 GeV have been commissioned at the ITEP (800 MeV) in Moscow, Russia,⁴ the IHEP (70 GeV) in Protvino, Russia,^{5,6} the BNL (24 GeV) in Brookhaven, USA,⁷ and GSI (4.5 GeV) in Darmstadt, Germany.⁸ Efforts on constructing a facility at the IMP in Lanzhou, China, have been made but not yet been realized;^{9–11} however, the diagnostics may be implemented for future warm dense matter experiments at the HIAF in Huizhou, China.¹²

The custom radiography lens system required for this technique, a magnetic quadruplet—commonly known as *Russian quadruplet*¹³—allows for a flexible adjustment of magnification and image contrast and provides second-order chromatic aberration correction.^{1,14} It is driven in a way so that the measured proton transmission distribution at the detector position is directly related to nuclear interactions and multiple Coulomb scattering (MCS) in the target investigated.¹⁴ Therefore, image contrast is dependent on the scattering angle of the protons and can thus be translated to areal densities using an approximation of the Molière scattering theory.^{15,16}

In order to enhance the capabilities of this technique, several advancements have been developed over the past years. For imaging of low-density processes such as, e.g., turbulent mixing of gases, inverted collimation can be used to enhance the contrast of low density features.¹⁷ For this, protons with both large and small scattering angles are removed from the beam simultaneously, leaving only protons that have scattering angles corresponding to the density window investigated. Furthermore, dark-field radiography has been developed, which is capable of significantly enhancing image contrast at the cost of lower proton intensity.¹⁸

The performance of lens-based radiography facilities is dependent on the overall length of the magnetic imaging lens itself (see Sec. II), and as such, compact and strong quadrupoles are desirable for such systems. Apart from superconducting magnet technology, the highest field gradients can be achieved with permanent magnet quadrupole (PMQ) lenses. Therefore, several systems of this kind, e.g., at GSI in Germany, were developed¹⁹ and built⁸ using the highest energy-density NdFeB permanent magnet materials. Such quadrupoles are based on multi-layer Halbach-style arrays assembled from individual permanent magnet elements with different magnetic orientations.²⁰ Despite providing the highest field gradients at very compact dimensions, those magnetic assemblies have been proven to be subject to strong self-demagnetization due to radiation damage through interaction with the scattered high energy primary protons and secondary particles.^{8,21,22} As this effect also leads to a severe degradation of the image quality, the new PRIOR-II facility relies on compact high-gradient and radiation-resistant normal conducting magnets, which provide constant field quality and enhanced tuning capabilities. Such systems based on

electromagnets are also especially suitable for applications in very confined spaces, where PMQ lenses pose a significant disadvantage as they require movement along the beam axis for focusing multiple beam energies.

The new PRIOR-II facility at GSI is designed to take advantage of the most recent developments in the field by employing a set of custom high-gradient normal conducting magnets, which are specifically designed to suppress high-order parasitic multipole field components at nominal working currents for 4–5 GeV protons (about 80%–90% load). This enables a sub-10 μm design spatial resolution, allowing the probing of fine structural effects in dynamic shock-wave experiments, which currently cannot be visualized at other operational facilities. Furthermore, contrary to present normal conducting magnet based radiography designs relying on just two power supplies, the PRIOR-II quadrupole magnets are driven by four individual power supplies with a high current stabilization providing an increased tuning capability of the system and allowing for the correction of even the smallest mechanical and magnetic deviations. Combined with the proton pulse structure provided by the SIS-18 synchrotron at GSI (up to four individual bunches within about 600–800 ns), PRIOR-II represents a new, valuable instrument for research on various challenging areas in the fields of materials science and plasma physics.

II. DESIGN AND CONSTRUCTION

A. Ion optical design

In order to understand the challenges of the ion optical design, a brief introduction of the underlying beam physics is necessary.

Let the coordinates of a particle at the object plane of an imaging system be $\mathbf{x} = \{x_1, x_2, \dots, x_6\}$, where according to common (e.g., COSY INFINITY code^{23,24}) notation,

$$\begin{aligned} x_1 &= x, & x_2 &= a = p_x/p_0, \\ x_3 &= y, & x_4 &= b = p_y/p_0, \\ x_5 &= l = -\frac{(t-t_0)v_0\gamma}{1+\gamma}, & x_6 &= k = \frac{K-K_0}{K_0}, \end{aligned} \quad (1)$$

where x and y are the horizontal and vertical positions, respectively; p_x and p_y are the horizontal and vertical momentum components, respectively; and p_0 , K_0 , v_0 , t_0 , and γ are the momentum, kinetic energy, velocity, time of flight, and total energy over m_0c^2 of the reference particle, respectively. These coordinates are canonical. After passing through the lens system, the coordinates of a particle at the detector (image) plane are $\mathbf{X} = \{X_1, X_2, \dots, X_6\}$. The final coordinates, \mathbf{X} are related to initial coordinates, \mathbf{x} by a transfer map (Taylor expansion) $\vec{\mathcal{M}} = \{\mathcal{M}_1, \mathcal{M}_2, \dots, \mathcal{M}_6\}$,

$$X_k = \mathcal{M}_k \circ \mathbf{x} = \sum_{\{i_i\}, \sum i_i \leq N} \mathcal{M}_{k,\{i_i\}} x_1^{i_1} x_2^{i_2} \dots x_6^{i_6}, \quad (2)$$

where N is the order of the transfer map. The elements $\mathcal{M}_{k,\{i_i\}}$ of the vectors \mathcal{M}_k are proportional to the partial derivatives of the final coordinate X_k with respect to the corresponding initial coordinates $\{x_i\}$, e.g., the second-order element $\mathcal{M}_{1,\{2,6\}} \propto \frac{\partial X_1}{\partial a \partial k}$.

Due to a finite relative initial energy spread of the SIS-18 beam²⁵ σ_k of about 10^{-3} , as well as energy loss straggling in the target, high-order chromatic effects have to be considered. The most

dominant aberrations are the second-order chromatic aberrations,² namely, position- and angle-dependent aberrations, which can be described for X_1 through the second-order transfer map elements $\mathcal{M}_{1,\{1,6\}}$ and $\mathcal{M}_{1,\{2,6\}}$. Assuming that the (x, a) and (y, b) phase space planes of the ion optical system are decoupled, this yields for the X_1 coordinate (x -coordinate) from Eq. (2),

$$X_1 = \mathcal{M}_{1,\{1\}} \cdot x + \mathcal{M}_{1,\{2\}} \cdot a + \mathcal{M}_{1,\{1,6\}} \cdot x \cdot k + \mathcal{M}_{1,\{2,6\}} \cdot a \cdot k + \dots \quad (3)$$

The imaging condition for proton radiography is equivalent to point-to-point focusing, where the final position of a proton X is independent from the initial angle, a , hence

$$\mathcal{M}_{1,\{2\}} = 0, \quad \mathcal{M}_{3,\{4\}} = 0, \quad (4)$$

and the first-order elements $\mathcal{M}_{1,\{1\}} \equiv M_x$, $\mathcal{M}_{3,\{3\}} \equiv M_y$ are the geometrical magnifications of the imaging system.

Furthermore, by preparing the incoming beam at the object location using upstream magnetic quadrupoles, so that the correlation coefficients (beam convergence or divergence angles) fulfill the relations,

$$W_x = \frac{\langle xa \rangle}{\langle x^2 \rangle} = -\frac{\mathcal{M}_{1,\{1,6\}}}{\mathcal{M}_{1,\{2,6\}}}, \quad (5)$$

$$W_y = \frac{\langle yb \rangle}{\langle y^2 \rangle} = -\frac{\mathcal{M}_{3,\{3,6\}}}{\mathcal{M}_{3,\{4,6\}}},$$

the position-dependent second-order chromatic aberration terms $\mathcal{M}_{1,\{1,6\}}$ and $\mathcal{M}_{3,\{3,6\}}$ vanish as well. This is called *chromatic matching*^{1,26} and crucial for eliminating the most significant image distortions. As the remaining second-order angle-dependent terms cannot be canceled by any means, it is an intrinsic property of the magnetic lens system, which is often referred to as *chromatic length*^{1,26} C ,

$$C_x = \frac{\mathcal{M}_{1,\{2,6\}}}{M_x}, \quad C_y = \frac{\mathcal{M}_{3,\{4,6\}}}{M_y}. \quad (6)$$

The *chromatic length* is a suitable parameter, which can be employed for optimizing the performance of radiographic lens systems, as shown in Fig. 1. For practical purposes, one can estimate the spatial resolution performance of a proton microscope due to the second-order chromatic aberration only just as

$$R_{x,y}^C \approx 0.479 \cdot C_{x,y} \cdot \theta_c \cdot \sigma_k, \quad (7)$$

where θ_c is the acceptance of the collimator at the Fourier plane of the system providing image contrast due to the MCS in the object and $\sigma_k = \sqrt{\langle k^2 \rangle}$ is the total beam energy spread after an object. The coefficient 0.479 is due to the assumption that the collimator acceptance angle is matched to an object causing a normally distributed MCS with $\sigma_{a,b}$ so that $\theta_c \approx \sigma_{a,b}$. The approximation in Eq. (7) is called *chromatic resolution*; an example is presented in Table II, where it is calculated for several configurations of the PRIOR-II facility. If the beam after an object has a significant energy spread σ_k and the collimator acceptance angle θ_c is not too large, the chromatic resolution is expected to be the dominating term.

In order to reduce the *chromatic length* and, therefore, increase the performance of the imaging system, the drifts L_1 through L_3 between the individual magnetic elements and the lengths QL_1 and QL_2 of the elements itself have to be minimized (see Fig. 1). As the object to image distance L_{tot} at the HHT (high energy, high temperature) experimental area at GSI and at the FAIR facility is fixed to 9.5 and 20.0 m, respectively, the last drift L_4 is defined by the chosen parameters of the system and does not need to be considered. Reducing both, drifts and element lengths, always comes at the cost of higher quadrupole field gradients and steeper beam slopes W_x and W_y from Eq. (5), which makes it harder to achieve the conditions for *chromatic matching* with the upstream elements and also reduces the beam size at the object location and, therefore, the available field of view (FOV).

The ion optical design of the PRIOR-II facility was first optimized for fielding at the existing HHT experimental area of the GSI for proton energy of 4 GeV. The final design was then transferred

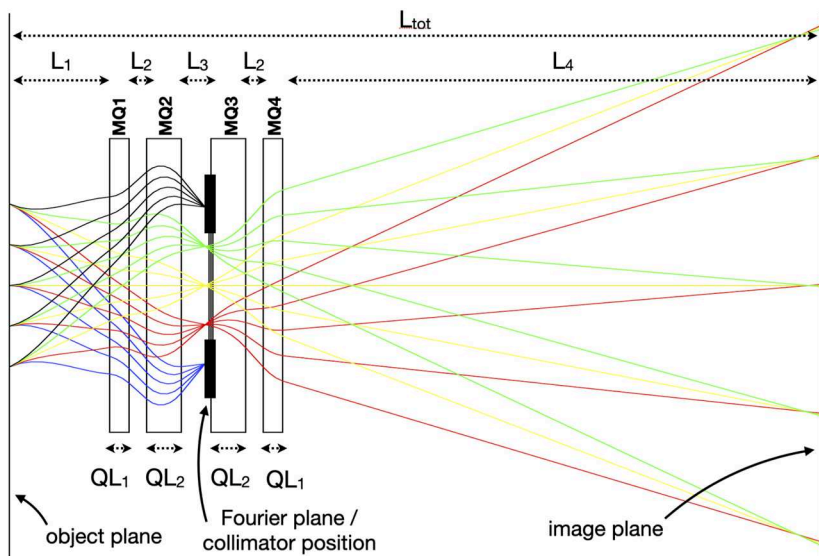


FIG. 1. General schematics of a magnifying magnetic quadruplet or *Russian quadruplet* for particle or proton imaging purposes. A beam envelope in the horizontal x -plane for a D-F-D-F configuration of the lens is shown (calculated in COSY INFINITY); trajectories with large scattering angles are sorted out in the Fourier plane using a collimator.

to the FAIR facility and underwent a performance evaluation with 5 GeV protons. As a variation of the lengths of the magnetic elements generally has a larger effect on the *chromatic length* than a variation of the drift lengths, the optimization procedure was carried out by first fixing the drifts L_x to a mechanically reasonable minimum and then reducing the length QL_x of the quadrupoles until 90% load for the maximum pole tip field of about 1.3 T was reached. This also ensured compatibility at FAIR with even higher energy protons from the SIS-100 synchrotron. Furthermore, the length-ratio between long inner and short outer magnetic quadrupoles MQ2, MQ3 and MQ1, MQ4, respectively, was preserved (1.625:1) to ensure equal load on all elements. This optimization procedure was performed for multiple pole tip radii from 15 mm up to 30 mm. As the corresponding angular acceptance or FOV of the setup showed a significantly stronger dependence on the aperture radius than the *chromatic length*, a design with a larger aperture was favored to increase the maximum FOV for future physics experiments at GSI and at FAIR.

B. Ultra-high-gradient normal conducting quadrupole lenses

Following the ion optical optimization procedure, the main technical parameters of the PRIOR-II quadrupole magnets were fixed and are presented in Table I. It is to be noted that the chosen maximum flux density of 1.3 T on the pole tip is rather high as normal conducting quadrupoles usually do not exceed 0.9–1.0 T pole tip field. The saturation effects in the PRIOR magnets may, therefore, significantly distort the field distributions. At the same time, an excellent field quality is required within the good field area of the magnets within a wide range of the field gradients for different proton energies. Among other considerations, these contradictory requirements demand careful designing of the yoke geometry including the pole tip shape, coil configuration, and the end chamfer profile.

The magnet design of the PRIOR-II system was carried out in a multi-stage process starting with an optimization of the pole tip shape described in the studies in Refs. 27–29. The scalar magnetic potential $U(r, \theta)$ in the magnet aperture may be expressed by

a Fourier expansion in polar coordinates, with g being the pole tip radius, as shown in the following equation:

$$U(r, \theta) = U_2 \left(\frac{r}{g} \right)^2 \cos(2\theta) + U_6 \left(\frac{r}{g} \right)^6 \cos(6\theta) + \dots \quad (8)$$

For a system with the quadrupole fourfold symmetry, only the terms U_2 , U_6 , and U_{10}, \dots appear in the expansion. Moreover, for the ideal magnet, only the first term in Eq. (8) with the amplitude of U_2 is not vanishing. In practice, the ideal field configuration is disturbed by the finite dimensions of the pole, by the influence of coils and nonlinear magnetic properties of the steel, all of which excite high-order parasitic harmonics. Amplitudes of these harmonics can be partially suppressed by a proper choice of the pole tip shape. The main principles of the performed optimization procedure are based on the idea that the pole border line may be described in terms of a Fourier series and the field distribution in the magnet aperture. A strong correlation between amplitudes of corresponding expansions provides conditions for a fast and robust convergence of the pole shape optimization procedure.²⁹ Such an optimization option for the multipole magnets has been integrated into the software MULTIMAG²⁷ developed for computing magnetic fields in accelerator magnets on the basis of finite element method. The goal function for the optimization procedure is formed as a set of the desired field harmonics in the aperture.

While for normal conducting quadrupole beam line magnets, only the main harmonic U_2 is usually assumed to be not equal to zero; magnets that operate in deep saturation, such as the PRIOR-II magnets, pose a challenge for a magnet design. According to the main requirements to the developed magnets, the flux density in the iron core will strongly saturate the pole material. Consequently, a distortion of the field distributions at maximum excitation currents exceeds acceptable margins. It is possible to reformulate the requirements to the field quality in the magnet aperture in terms of maximum acceptable amplitudes of the field harmonics at the border of the good field area. A series of numerical experiments demonstrated that saturation effects change mainly the amplitude of the first non-quadrupole harmonic U_6 (see Fig. 4). Therefore, it was decided to find a pole tip profile, which initially induces the sixth harmonic of the flux density distribution with the maximum acceptable amplitude. Saturation of the iron reduces this amplitude to zero in intermediate fields and reverses the sign of the amplitude (or more accurately—changes the phase of the corresponding term in Fourier series by 180°). In such a way, we achieved the maximum possible range of the field gradient variation. To further widen this range, an air slot was introduced for the pole of the magnet (Fig. 2 left). Such an arrangement—commonly known as Purcell filter³⁰—produces the effect of “negative shimming” in the case of saturated pole and properly corrects the field distribution for the case of the maximum excitation current. The parameters of the hole are as follows: the diameter is 10 mm and the distance to the pole surface is 13 mm.

Based on the 2D cross section described above, a 3D model of the PRIOR-II magnets has been built for further optimization. This model has been analyzed using OPERA 3D³¹ software (Fig. 2 right). Optimal parameters of the end chamfers (the inclination angle of 60° and the length of 6 mm) provide similar correction of the field distributions in the magnet aperture for all excitation currents in the

TABLE I. PRIOR-II technical design parameters. The effective lengths and maximum effective fields (integrated gradients) are given at the maximum specified current.

	MQ1, MQ4	MQ2, MQ3
Pole tip radius	30 mm	
Good field radius	25 mm	
Max. pole tip field	1.3 T	
Field quality	$\pm 4 \times 10^{-4}$ rel. units	
Geom. length	400 mm	650 mm
Eff. length	(415 ± 2) mm	(658 ± 2) mm
Weight	1200 kg	1800 kg
Turns per coil	15	
Max. current	1700 A	
Total power	$38.6 \text{ kW} \pm 10\%$	$52.0 \text{ kW} \pm 10\%$
Max. gradient	42 T/m	42.8 T/m
Max. effective field	17.4 T	28.2 T

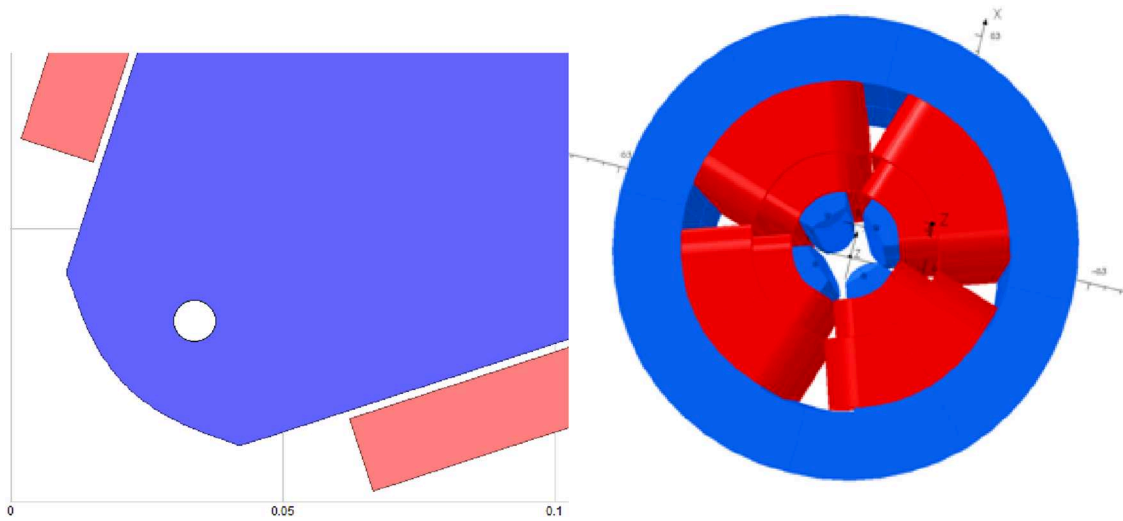


FIG. 2. Cross section of the pole tip of the PRIOR-II quadrupole magnet (left) and corresponding 3D model of the final magnet (right).

coil. The chosen final pole chamfer ensured a similarity between the field distributions in the central cross section and the corresponding average flux density $G = \int G(z)dz/L$, where L is the yoke length. The integral field quality in the magnet aperture is shown in Fig. 3.

The dependency of the parasitic high-order field harmonics in the magnet aperture on the magnitude of the pole tip field is shown in Fig. 4. It confirms the initial assumption that the saturation effects affect mostly the sixth harmonic amplitude, which was used at the stage of pole shape optimization. One can see that the maximum amplitudes of undesired field harmonics in the magnet aperture shown in Fig. 3 do not exceed the required limits presented in Table I.

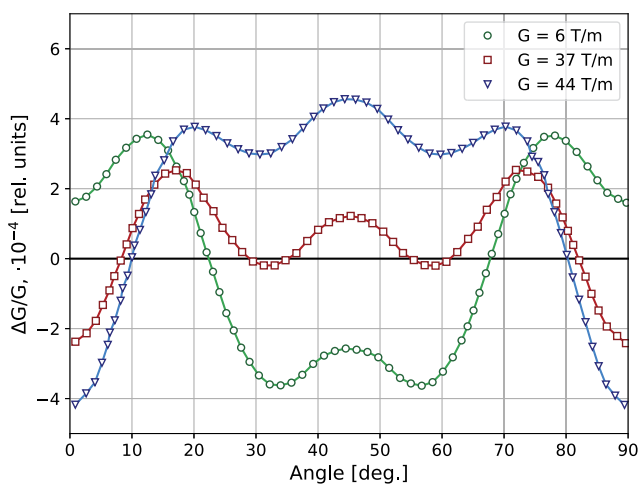


FIG. 3. Integral flux density distribution in the aperture at the border of the good field area for different flux density levels for the 400 mm long magnet.

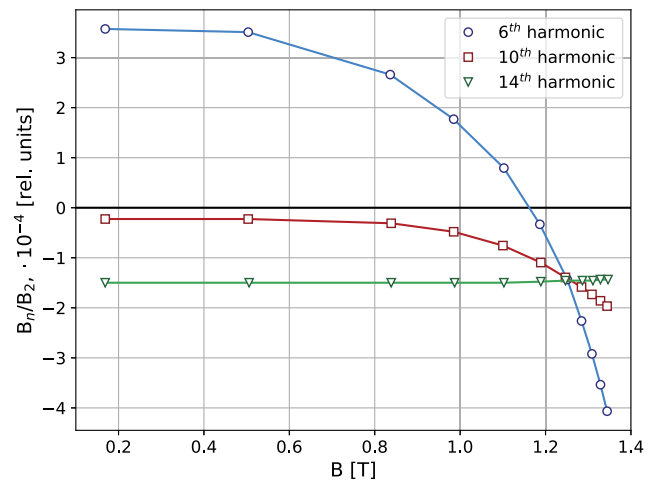


FIG. 4. Flux density harmonics at the border of the good field area as functions of the pole tip field magnitude.

C. Final design parameters

As the result of the design work described above, the key parameters of the PRIOR-II proton microscope are presented in Table II for use at the present HHT experimental area with up to 4 GeV protons from the SIS-18 synchrotron as well as at the APPA (Atomic, Plasma Physics and Applications) cave at the future FAIR facility with up to 5 GeV from the SIS-100 synchrotron.

Due to different geometrical constraints at both experiment locations, the main difference between the two use cases is the available object-to-image distance, L_{ot} , which mostly affects the systems' magnification and, therefore, the required detector size. Both scenarios show very similar performance in terms of the available FOV and

TABLE II. Ion optical design and performance of PRIOR-II at GSI and FAIR. The spatial resolution performance has been calculated in the object plane under the assumption that downstream of the object the energy and angular spreads of the beam are $\sigma_K = 7 \times 10^{-4}$ and $\sigma_{a,b} \approx \theta_c$, respectively.

	FAIR		GSI	
Geometry				
Object to image distance, L_{tot}	20.0 m		9.5 m	
Object to matching distance, L_0	1.0 m		1.0 m	
Stand-off, L_1	0.5 m		0.5 m	
Outer gaps Q1–Q2 and Q3–Q4, L_2	0.1 m		0.1 m	
Middle gap Q2–Q3, L_3	0.5 m		0.4 m	
Distance to the image, L_4	16.7 m		6.3 m	
Optical properties				
Reference energy, E_o	5000 MeV		4000 MeV	
Normalized RMS emittance, $\epsilon_x \times \epsilon_y$ (mm mrad)	6.25×2		6.25×2.5	
Magnification, M	8.03		3.49	
Chromatic length, $C_x \times C_y$ (m)	2.66×5.04		2.77×5.24	
Matched beam slope, $W_x \times W_y$ (mrad/mm)	-0.4849×-0.2270		-0.5292×-0.1990	
Performance				
Collimator acceptance, θ_c (mrad)	2	5	2	5
Field of view, $FOV_x \times FOV_y$ (mm)	30×52	29×48	30×57	30×54
Chromatic resolution, $R_x^C \times R_y^C$ (μm)	1.8×3.4	4.5×8.5	1.9×3.6	4.7×8.9

the spatial resolution. This indicates that the best achievable spatial resolution for the given σ_K and θ_c [see Eq. (7)] is limited by the intrinsic ion-optical aberrations of the magnifier only. It is to be noted that the actual spatial resolution is likely to be limited by other factors, e.g., by the available detector resolution discussed in more detail in Sec. III A.

The proton microscope is first fielded and commissioned at the HHT experimental area at GSI. The ion-optical layout of the corresponding HHT beam line section, including the *matching* section upstream of the object location as well as the imaging quadruplet, is shown in Fig. 5 alongside the envelopes of the matched beam. Here, mostly the apertures of the last two matching quadrupoles are

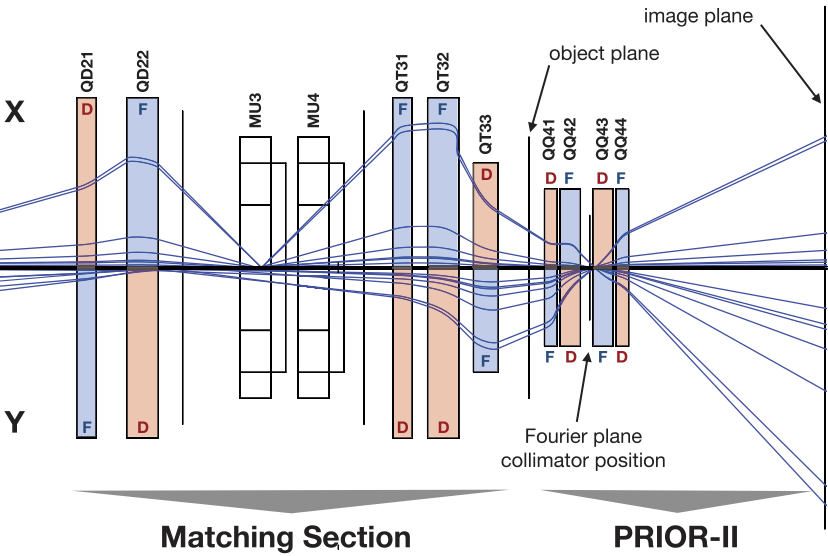


FIG. 5. Ion-optical layout of the HHT beam line at GSI with the PRIOR-II microscope in D–F–D–F configuration. The beam envelopes (above the axis—horizontal and below the axis—vertical) show a matched beam configuration calculated and plotted with COSY INFINITY. Element names are printed according to the GSI nomenclature, hence MU—dipole, QD—quadrupole duplet, QT—quadrupole triplet, and QQ—quadrupole quadruplet.



FIG. 6. PRIOR-II setup fielded at the HHT experimental area at GSI. Upstream view from behind the last (short) quadrupole of the imaging quadruplet toward the Fourier plane and the object plane. The last (dark blue) quadrupole of the matching section in front of PRIOR-II (see Fig. 5) can be seen on the left-hand side of the picture.

limiting the FOV of the system. The maximum achievable magnification of the system is given by the total length available at the HHT area, $L_{tot} = 9.5$ m. A picture of the setup at the HHT area captured during the commissioning run is shown in Fig. 6.

The imaging quadruplet is driven in a D-F-D-F instead of the common F-D-F-D configuration, i.e., the first PRIOR quadrupole lens is defocusing in the horizontal plane (see Fig. 5). This makes the matching by the existing upstream HHT beam line quadrupoles more efficient, requiring a steeper matching angle W_x [Eq. (5)] and also leads to a smaller horizontal chromatic length $C_x \approx 0.5C_y$ and a larger FOV in the vertical direction, which is preferable for foreseen dynamic experiments.

The PRIOR-II design for both use cases allows for a certain degree of flexibility: the performance and properties of the magnifier can be adapted to an experiment by adjusting the L_1 and L_4 distances, especially—at FAIR. The FOV can also be enlarged by increasing the L_3 distance at the cost of slightly degraded spatial resolution of the system. However, as the geometrical changes to the system will also affect the position of the Fourier plane with respect to the mechanical collimator position in the beam pipe, the density reconstruction performance of the system needs to be re-checked for a particular geometry.

III. TUNING AND OPERATIONAL COMMISSIONING

A. Lens tuning and spatial resolution performance analysis

Prior to performance measurements and physics experiments, the working point of the radiographic system needs to be determined and adjusted to correct for first-order errors of the ion optics introduced by, e.g., mechanical deviations from component alignment, magnetic field uniformity, magnetic field errors introduced by overlapping fringes, and hysteresis effects (iron yoke saturation). Those errors may lead to longitudinally separated focal planes in x and y , thus degrading the spatial resolution performance at the physical image plane and producing an undesirable slightly astigmatic imaging. It is possible to correct for those errors by introducing so-called eigenscans. By varying the individual magnet currents in a specific pre-calculated way, it is possible to decouple horizontal and vertical focusing [Eq. (4)] while still preserving the stigmatic imaging conditions ($\mathcal{M}_{1,\{1\}} = \mathcal{M}_{3,\{3\}} = M$). This requires at least three degrees of freedom or “3 knobs” (independent magnets’ currents). Here, the PRIOR-II setup with four individually controlled power supplies has a significant advantage compared to 2-knob radiographic systems with just two power supplies, which can only be tuned accepting a trade-off between the ideal spatial resolution performance and stigmatic imaging. A comparison between the simple 2-knob with a correction for $\mathcal{M}_{1,\{2\}}$ to prevent the x - and y -magnifications from drifting apart too far and the 3-knob eigenscan method for PRIOR-II calculated in COSY INFINITY is shown in Fig. 7. To simplify matters, we only consider the “EigenX” scans with the fixed focus location in the x -plane. However, all the calculations and measurements were carried out analogously for the y -plane as well.

From the graphs shown in Fig. 7 it is clear, that while keeping the first-order imaging conditions $\mathcal{M}_{1,\{2\}} = \mathcal{M}_{3,\{4\}} = 0$ and minimizing the corresponding second-order chromatic terms from Eq. (7), the best spatial resolution performance with the stigmatic imaging $M_x = M_y$ is dependent on the second-order terms and, therefore, identical to the design parameters presented in Table II. In practice, several other factors, such as previously mentioned magnetic field non-uniformity, overlapping fringe fields, and also physical limitations of the detector system, may play a significant role as well.

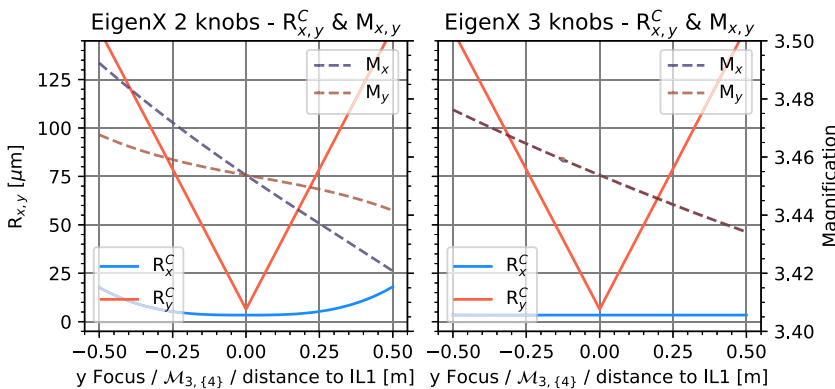


FIG. 7. Spatial resolution performance and magnifications for EigenX scans (horizontal focus fixed) for a 2-knob system (left) with artificial third-order correction factor for $\mathcal{M}_{1,\{2\}}$ to prevent the magnifications from drifting apart and a 3-knob system (right). For the 2-knob system, we shift the y focus by varying the two parameters A, B , where $MQ1 = A$, $MQ2 = -B$, $MQ3 = B$, and $MQ4 = -A$ while allowing for a small deviation $\mathcal{M}_{1,\{2\}} \neq 0$. For the 3-knob system, we have chosen A, B, C , where $MQ1 = A$, $MQ2 = B$, $MQ3 = C$, and $MQ4 = -A$.

In order to quantify the performance in an experiment setting, one has to find a definition for the spatial resolution performance of a radiographic setup. As ultra-fine and thin structures commonly used in conventional light optics for measuring the modular transfer function (MTF) would not produce sufficient image contrast when imaged with high energy protons, we instead consider the width of the horizontal/vertical sharp edge transitions of a thick object, i.e., a tungsten block, which is similar to a line spread function (LSF). A normal edge transition can be fitted with the error function,

$$f(x) = a + b \cdot \operatorname{erf}\left(\frac{x - \mu}{\sigma \cdot \sqrt{2}}\right), \quad (9)$$

as shown in Fig. 8. While Eq. (9) is useful for the quantifying particle radiography images, it may not fully describe possible over-/undershoot due to limning¹ or tilted profiles due to the non-flat shape of the incoming proton beam distribution. For those specific scenarios, a “double” error function fit—a convolution of two error functions—can help for practical reasons.

The PRIOR-II setup has been tuned using consecutive eigen-scan procedures with 4 GeV protons, as described above and shown in Fig. 7 (right). The best measured spatial resolution performance on a tungsten edge target [see Fig. 8 (left)] was determined to be $R_x = 70.1$ (20.1) μm and $R_y = 67.0$ (19.2) μm in the image (object) planes, respectively, with the system magnification of $M \approx 3.49$ (see Table II). As this is about a factor of three worse than the calculated theoretical ion-optical spatial resolution $R_{x,y}^C$ from Table II, we need to consider the influence of the used detector setup on the measured performance as well.

The spatial resolution of a detector depends on the pixel resolution of the camera used, on the resolution of the optical lenses mapping the image of the scintillator screen on the camera’s sensor, and on the point spread function (PSF) width of the scintillator screen itself. The detector setup at GSI consists of a 5.5 Mp CMOS camera (PCO Edge) with 6.5 μm pixel pitch and a Schneider Kreuznach Emerald 100 mm F2.8 lens. The scintillation screen was a 2 mm thick slab of doped monolithic CsI(Tl) from Proteus Inc. with about 520 nm peak wavelength emission. With the detector geometry at GSI, the theoretical limit of the camera’s CMOS sensor translates to a pixel pitch of 20 (5.7) μm at the image (object) planes,

correspondingly. However, actual measurements with the identical detector geometry and a razor blade target instead of the scintillation screen illuminated uniformly by a green LED with 520 nm peak wavelength showed a spatial resolution limit of 30–35 (8.6–10) μm attributed to the alignment of the optical detector system at the given wavelength.

While attempts have been made to formulate PSF models for the interaction of x rays and low energetic particles with scintillator screens,³² no data exist for imaging applications with high energy protons. We have measured the spatial resolution performance of various scintillation materials at different thicknesses with the method described above, where monolithic CsI(Tl) showed a spatial resolution decrease per thickness unit of 5.9 $\mu\text{m}/\text{mm}$. However, the observed limit of about 20.0 μm at the object plane is reached at 2.0 mm scintillator thickness already; a further decrease in the thickness did not improve the observed results.

The findings are confirmed through a second set of measurements completely replacing the detector setup with GAFchromic EBT3 films, which are specified for an intrinsic resolution of 25.0 μm . Here, a spatial resolution of 60–70 μm was measured at the image plane indicating that the observed discrepancy between spatial resolution measurements and the theoretical ion-optical chromatic resolution limit does not originate from detector limitations. We assume that a more detailed description of the ion-optical spatial resolution performance considering all sorts of non-uniformities in the magnetic field distribution of the magnetic quadrupole lenses as well as higher-order ion-optical aberrations is required to describe the observed performance of the system. The ongoing further analysis of the system’s performance will help push the boundaries of what can be achieved with high-energy charged particle radiography setups.

B. Commissioning for physics experiments

While future applications of PRIOR-II certainly require the best possible spatial resolution performance, another key parameter is the capability to precisely reconstruct the areal density and—for simple target geometries—volume density distribution in dynamic experiments. As briefly mentioned in Sec. I, this is possible as the image contrast is introduced mainly through collimation at the

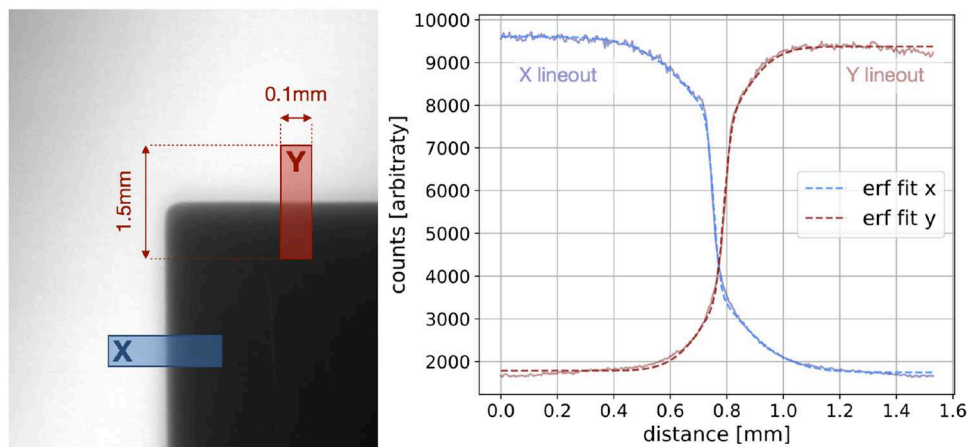


FIG. 8. Spatial resolution measurement on an image of a 20 mm-thick tungsten edge target (left). In order to compensate for geometrical alignment errors affecting the edge transition, both considered edges of the target were slightly rolled with a large ($r = 5.0$ m) radius. Two box selections (x—blue and y—red) with dimensions of 20×300 px² (0.1×1.5 mm²) were chosen; error functions [Eq. (9)] were fitted to the lineouts to determine the RMS spatial resolutions at the edge transition, $\sigma_x \approx \sigma_y \approx 20$ μm .

Fourier plane of the system, where the protons after penetrating a target are sorted radially by their angle or transverse momentum a, b (also see Fig. 1). This angle is composed of the initial proton angular distribution with the width θ_0 before the interaction with a target as well by the MCS angle $\theta(z)$ after the target of a thickness z , which can be obtained from the Molière scattering theory.¹⁶

By dividing the target image through the undisturbed proton beam distribution, one obtains the proton transmission image, which—given a linear response of the detector—is directly related to inelastic and elastic proton-target interaction processes, namely, particle removal through nuclear collisions (NC) and MCS. This model for radiographic density reconstruction has already been discussed in detail in other studies.^{1,8,33} We can describe the beam transmission through a target as

$$T(z) = \underbrace{\frac{1}{T_0}}_{\text{NC}} \cdot e^{-z/\lambda_{nc}} \cdot \underbrace{\left(1 - e^{-\frac{\theta_c^2}{2(\theta^2(z) + \theta_0^2)}}\right)}_{\text{MCS}}. \quad (10)$$

Here, $T_0 = 1 - e^{-\theta_c^2/2\theta_0^2}$ is the transmission of the undisturbed beam without a target, and λ_{nc} is the nuclear collision length of the target material.

We have evaluated the model in Eq. (10) for step wedge data captured with the PRIOR-II setup and a number of collimators from 2.5 mrad up to 5.0 mrad angular acceptance to ensure the validity of the model as well as to estimate and quantify the experimental areal density resolution reconstruction capabilities of the setup. It should be noted that the collimators for PRIOR-II are not ideally thin planes as shown in Fig. 1 but 100 mm thick elements made from a tungsten alloy. While this is not a sufficient amount of material to stop 2 GeV protons used for this study, it introduces sufficient parasitic beam scattering beyond the acceptance of the last two electromagnetic quadrupoles so that the interacting particles do not contribute to the final image anymore and do not affect the density resolution of the setup.

The transmission model has been fitted to the captured step wedge data to determine the initial proton angle θ_0 as well as

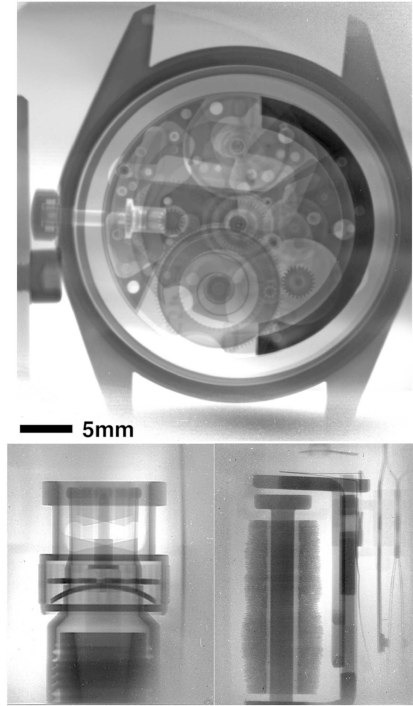


FIG. 10. Top panel: proton radiography of a mechanical wristwatch with a 3.5 cm diameter. As the watch is slightly larger than the maximum FOV of PRIOR-II at GSI, the picture is stitched together from two separate images (top and bottom). Bottom left: side view of a standard BNC plug. Bottom right: side view of an old mechanical relay. The winding of the coil is composed of 80 μm enameled copper wire; individual wire cross sections can be resolved.

the actual collimator acceptance θ_c , which is allowed to vary by $\pm 5.0\%$ due to possible physical misalignment of the beam on the geometrical axis and finite dimensions of the collimators extending off the Fourier plane. The resulting material and collimator

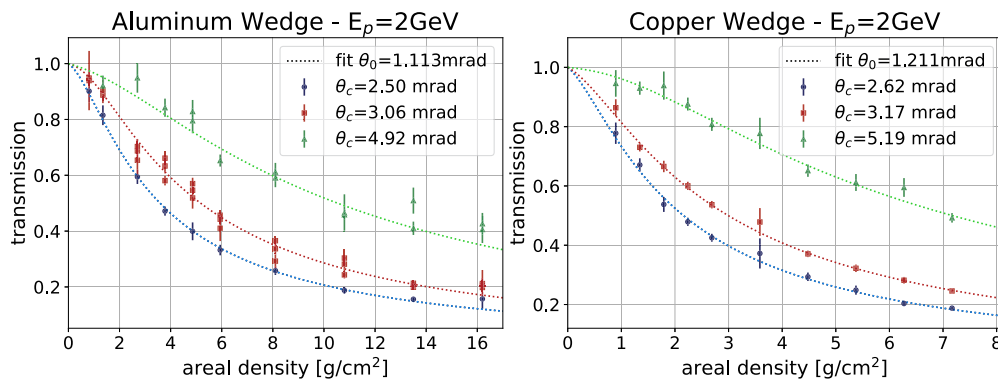


FIG. 9. Transmission data and corresponding fitted transmission curves for aluminum (left) and copper (right) step wedge targets imaged using collimators with 2.5, 3.0, and 5.0 mrad angular acceptances.

dependent transmission curves and the data points used for fitting are shown in Fig. 9. While the agreement of the model with the captured data is very good in general, we have observed a few outliers in the data, which are caused by an unstable beam profile distribution from the SIS-18 synchrotron. As discussed above, the particle scattering model describes proton transmission; therefore, each captured target image needs to be divided by an undisturbed proton distribution, which has to be acquired as a separate image. Due to shot-to-shot pointing fluctuations caused by slightly varying extraction angles from the SIS-18 synchrotron, these beam profiles may slightly differ from each other, consequently introducing small artificial areal density gradients in the final transmission image.

The overall density reconstruction accuracy, mainly affected through warped transmission images in the particular commissioning experiments, has been determined to be 1.9% for the 2.5 mrad collimator, 2.6% for the 3.0 mrad collimator, and 4.0% for the 5.0 mrad collimator. As per Eq. (10), the error is increasing for larger collimator acceptances θ_c .

In order to illustrate the capabilities of PRIOR-II, we have also captured radiographic images of various “complex” objects to showcase the capabilities of this technique, some of which are shown in Fig. 10.

IV. CONCLUSION AND OUTLOOK

Following the commissioning of the PRIOR-I prototype at GSI,⁸ the PRIOR-II proton radiography facility has been successfully designed, constructed, and fielded at the HHT experimental area of GSI, making use of the latest advancements in normal conducting magnet technology to maximize the overall performance of the system. PRIOR-II has already demonstrated a 20 μm spatial resolution and a sub-2% density reconstruction capability with 2–4 GeV protons during the commissioning run, establishing itself as a unique diagnostic device for international users.

With the future high-speed dynamic detector system consisting of an array of four intensified gated sCMOS cameras, which enable exposure times of 10–20 ns, it is especially suited for dynamic shock wave experiments, which require fast measurements with μm -scale spatial and ns-scale temporal resolutions while probing dense matter. The short exposure times are possible due to the intense proton pulses (5×10^9 – 8×10^{10} particles per pulse) from the SIS-18 synchrotron, which has also been demonstrated during the commissioning beam time measurements with single intensified cameras and fast plastic scintillators, allowing for sufficient radiography contrast even for high-areal-density experiments.

In addition to probing ultra-fast experiments, PRIOR-II is also capable of visualizing semi-dynamic processes in dense matter on a timescale of several milliseconds up to 8 s using a slow extracted beam from the SIS-18. Experiments of this type have been conducted at the Los Alamos National Laboratory;³⁴ however, the flexible timing of the SIS-18 synchrotron will enable a larger variety of such experiments especially for material science applications, e.g., melting of alloys and viscosity measurements under extreme conditions.

Due to complex ion-optical effects, the predicted ultimate spatial resolution performance of the PRIOR magnifier has not yet been

reached, which is a subject of ongoing theoretical investigations and future experiments.

ACKNOWLEDGMENTS

The authors acknowledge GSI's accelerator and technical teams for their support during the integration and commissioning of the PRIOR-II setup at GSI (D. Acker, M. Bevcic, H. Bräuning, T. Brühne, C. Clausen, E. Dierssen, C. Dorn, R. Fischer, J. Jöhnke, A. Junge, R. Haseitl, C. Hunkel, R. Lonsing, L. Lindig, A. Petit, I. Pschorn, C. Schmidt, M. Schwickert, K. Steiner, R. Vincelli, and B. Walasek-Höhne) as well as for the fine tuning of the GSI machines for the high energy and high intensity proton operation (W. Barth, Y. El-Hayek, D. Ondreka, P. Spiller, and J. Stadlmann).

The results presented here were obtained within the framework of the S440 and S488 experiments performed at the GSI Helmholtzzentrum fuer Schwerionenforschung, Darmstadt (Germany) in the frame of FAIR Phase-0. The authors acknowledge the support from BMBF under Grant No. 05P21RFFA2 for the S488 experiment. The publication is funded by the Open Access Publishing Fund of GSI Helmholtzzentrum fuer Schwerionenforschung GmbH.

The results presented in this paper are from a work conducted before February 24, 2022.

AUTHOR DECLARATIONS

Conflict of Interest

The authors have no conflicts to disclose.

Author Contributions

M. Schanz: Conceptualization (equal); Data curation (equal); Formal analysis (equal); Funding acquisition (equal); Investigation (equal); Methodology (equal); Project administration (equal); Resources (equal); Software (equal); Supervision (equal); Validation (equal); Visualization (equal); Writing – original draft (equal); Writing – review & editing (equal). **D. Varentsov:** Conceptualization (equal); Data curation (equal); Formal analysis (equal); Funding acquisition (equal); Investigation (equal); Methodology (equal); Project administration (equal); Resources (equal); Software (equal); Supervision (equal); Validation (equal); Visualization (equal); Writing – original draft (equal); Writing – review & editing (equal). **J. C. Allison:** Investigation (equal); Resources (equal). **V. Bag-noud:** Funding acquisition (equal); Supervision (equal). **R. Belikov:** Conceptualization (equal); Data curation (equal); Formal analysis (equal); Investigation (equal); Project administration (equal); Resources (equal); Software (equal); Supervision (equal); Validation (equal); Visualization (equal); Writing – review & editing (equal). **A. Blazevic:** Conceptualization (equal); Funding acquisition (equal); Project administration (equal); Resources (equal). **U. Eisenbarth:** Resources (equal); Software (equal). **M. S. Freeman:** Data curation (equal); Formal analysis (equal); Investigation (equal); Methodology (equal); Resources (equal); Supervision (equal); Writing – review & editing (equal). **R. Gavrillin:** Investigation (equal); Resources (equal); Software (equal). **J. Jacoby:** Funding acquisition (equal); Investigation (equal); Methodology (equal); Project administration (equal); Supervision (equal). **A. G. Kalimov:** Conceptualization (equal); Formal analysis (equal); Investigation (equal);

Methodology (equal); Validation (equal). **A. Khurchiev**: Investigation (equal); Resources (equal). **F. G. Mariam**: Conceptualization (equal); Formal analysis (equal); Investigation (equal); Methodology (equal); Resources (equal); Supervision (equal). **F. E. Merrill**: Conceptualization (equal); Methodology (equal); Resources (equal); Supervision (equal). **A. Müller-Münster**: Investigation (equal); Resources (equal); Software (equal). **L. P. Neukirch**: Formal analysis (equal); Resources (equal); Validation (equal). **S. Neff**: Project administration (equal); Resources (equal); Supervision (equal); Writing – review & editing (equal). **D. Nikolaev**: Investigation (equal); Methodology (equal); Resources (equal). **J. L. Schmidt**: Formal analysis (equal); Investigation (equal); Methodology (equal); Resources (equal); Software (equal); Validation (equal); Writing – review & editing (equal). **A. Skobliakov**: Investigation (equal); Resources (equal); Software (equal). **K. Weyrich**: Funding acquisition (equal); Investigation (equal); Project administration (equal); Resources (equal); Supervision (equal). **B. Winkler**: Conceptualization (equal); Funding acquisition (equal); Investigation (equal); Methodology (equal); Project administration (equal); Resources (equal); Supervision (equal); Writing – review & editing (equal). **B. Zielbauer**: Data curation (equal); Investigation (equal); Resources (equal); Software (equal).

DATA AVAILABILITY

The data presented in this publication are available on request from the authors M.S. and D.V.

REFERENCES

- ¹F. E. Merrill, “Flash proton radiography,” in *Reviews of Accelerator Science and Technology*, 8 (World Scientific Publishing, 2016), pp. 165–180.
- ²C. T. Mottershead and J. D. Zumbro, in *Particle Accelerator Conference, 1997* (IEEE, 1997), Vol. 2, pp. 1397–1399.
- ³N. S. P. King, E. Ables, K. Adams, K. R. Alrick, J. F. Amann, S. Balzar, P. D. Barnes, Jr., M. L. Crow, S. B. Cushing, J. C. Eddleman, T. T. Fife, P. Flores, D. Fujino, R. A. Gallegos, N. T. Gray, E. P. Hartouni, G. E. Hogan, V. H. Holmes, S. A. Jaramillo, J. N. Knudsson, R. K. London, R. R. Lopez, T. E. McDonald, J. B. McClelland, F. E. Merrill, K. B. Morley, C. L. Morris, F. J. Naivar, E. L. Parker, H. S. Park, P. D. Pazuchanics, C. Pillai, C. M. Riedel, J. S. Sarracino, F. E. Shelley, Jr., H. L. Stacy, B. E. Takala, R. Thompson, H. E. Tucker, G. J. Yates, H.-J. Ziock, and J. D. Zumbro, *Nucl. Instrum. Methods Phys. Res., Sect. A* **424**, 84 (1999).
- ⁴A. V. Kantsyrev, A. A. Golubev, A. V. Bogdanov, V. S. Demidov, E. V. Demidova, E. M. Ladygina, N. V. Markov, V. S. Skachkov, G. N. Smirnov, I. V. Rudskoy, A. P. Kuznetsov, A. V. Khudomyasov, B. Y. Sharkov, S. V. Dudin, S. A. Kolesnikov, V. B. Mintsev, D. N. Nikolaev, V. Y. Ternovoi, A. V. Utkin, D. S. Yuriev, N. S. Shilkin, V. E. Fortov, V. I. Turtikov, V. V. Burtsev, M. V. Zhernokletov, N. V. Zavialov, S. A. Kartanov, A. L. Mikhailov, A. V. Rudnev, M. V. Tatsenko, D. V. Varentsov, and L. M. Shestov, *Instrum. Exp. Tech.* **57**, 1 (2014).
- ⁵Y. M. Antipov, A. G. Afonin, A. V. Vasilevskii, I. A. Gusev, V. I. Demyanchuk, O. V. Zyat'kov, N. A. Ignashin, Y. G. Karshev, A. V. Larionov, A. V. Maksimov, A. A. Matyushin, A. V. Minchenko, M. S. Mikheev, V. A. Mirgorodskii, V. N. Peleshko, V. D. Rud'ko, V. I. Terekhov, N. E. Tyurin, Y. S. Fedotov, Y. A. Trutnev, V. V. Burtsev, A. A. Volkov, I. A. Ivanin, S. A. Kartanov, Y. P. Kuropatkin, A. L. Mikhailov, K. L. Mikhailyukov, O. V. Oreshkov, A. V. Rudnev, G. M. Spirov, M. A. Syrunin, M. V. Tatsenko, I. A. Tkachenko, and I. V. Khramov, *Instrum. Exp. Tech.* **53**, 319 (2010).
- ⁶V. V. Burtsev, A. I. Lebedev, A. L. Mikhailov, V. A. Ogorodnikov, O. V. Oreshkov, K. N. Panov, A. V. Rudnev, O. V. Shvirkii, M. A. Syrunin, Y. A. Trutnev, and I. V. Khramov, *Combust., Explos. Shock Waves* **47**, 627 (2011).
- ⁷C. Morris, K. Alrick, K. Buescher, D. Cagliostro, D. Clark, D. Clark, G. Cunningham, C. Espinoza, E. Ferm, R. Gallegos, S. Gardner, J. Gomez, N. Gray, G. Greene, A. Hanson, G. Hart, M. Hockaday, G. Hogan, N. Khalsa, and M. Wilke, *Defense Res. Rev.* **11**, 51–57 (2004).
- ⁸D. Varentsov, O. Antonov, A. Bakhmutova, C. W. Barnes, A. Bogdanov, C. R. Danly, S. Efimov, M. Endres, A. Fertman, A. A. Golubev, D. H. H. Hoffmann, B. Ionita, A. Kantsyrev, Y. E. Krasik, P. M. Lang, I. Lomonosov, F. G. Mariam, N. Markov, F. E. Merrill, V. B. Mintsev, D. Nikolaev, V. Panyushkin, M. Rodionova, M. Schanz, K. Schoenberg, A. Semennikov, L. Shestov, V. S. Skachkov, V. Turtikov, S. Udrea, O. Vasylyev, K. Weyrich, C. Wilde, and A. Zubareva, *Rev. Sci. Instrum.* **87**, 023303 (2016).
- ⁹H. Xiaozhong, Y. Guojun, and L. Chengjun, *High Power Laser Part. Beams* **20**(2), 297–300 (2008).
- ¹⁰Y. Guo-Jun, Z. Zhuo, W. Tao, H. Xiao-Zhong, L. Ji-Dong, S. Jin-Shui, and Z. Kai-Zhi, *Chin. Phys. C* **36**, 247 (2012).
- ¹¹L. Sheng, Y. Zhao, G. Yang, T. Wei, X. Jiang, X. Zhou, R. Cheng, Y. Yan, P. Li, J. Yang *et al.*, *Laser Part. Beams* **32**, 651 (2014).
- ¹²R. Cheng, Y. Lei, X. Zhou, Y. Wang, Y. Chen, Y. Zhao, J. Ren, L. Sheng, J. Yang, Z. Zhang, Y. Du, W. Gai, X. Ma, and G. Xiao, *Matter Radiat. Extremes* **3**, 85 (2018).
- ¹³A. D. Dymnikov, T. Y. Fishkova, and S. Y. Yavor, *Sov. Phys. Tech. Phys. - USSR* **10**, 340 (1965).
- ¹⁴C. L. Morris, N. S. P. King, K. Kwiatkowski, F. G. Mariam, F. E. Merrill, and A. Saunders, *Rep. Prog. Phys.* **76**, 046301 (2013).
- ¹⁵G. R. Lynch and O. I. Dahl, *Nucl. Instrum. Methods Phys. Res., Sect. B* **58**, 6 (1991).
- ¹⁶B. Gottschalk, A. Koehler, R. Schneider, J. Sisterson, and M. Wagner, *Nucl. Instrum. Methods Phys. Res., Sect. B* **74**, 467 (1993).
- ¹⁷M. S. Freeman, J. Allison, M. Andrews, E. Ferm, J. J. Goett, K. Kwiatkowski, J. Lopez, F. Mariam, M. Marr-Lyon, M. Martinez, J. Medina, P. Medina, F. E. Merrill, C. L. Morris, M. M. Murray, P. Nedrow, L. P. Neukirch, K. Prestidge, P. Rigg, A. Saunders, T. Schurman, A. Tainter, F. Trouw, D. Tupa, J. Tybo, W. Vogan-McNeil, and C. Wilde, *Rev. Sci. Instrum.* **88**, 013709 (2017).
- ¹⁸M. S. Freeman, J. C. Allison, E. F. Aulwes, B. A. Broder, M. G. Davis, M. Espy, P. E. Magnelind, F. G. Mariam, L. I. Martinez, J. J. Medina, W. Z. Meijer, F. E. Merrill, C. Morris, L. P. Neukirch, K. P. Prestidge, A. Saunders, T. Schurman, R. B. Sidebottom, A. M. Tainter, Z. Tang, F. R. Trouw, D. Tupa, J. L. Tybo, and C. H. Wilde, *Appl. Phys. Lett.* **117**, 144103 (2020).
- ¹⁹A. V. Kantsyrev, V. S. Skachkov, V. A. Panyushkin, A. A. Golubev, A. V. Bogdanov, A. V. Bakhmutova, E. M. Ladygina, N. V. Markov, O. S. Sergeeva, V. S. Skachkov, A. I. Semennikov, V. I. Turtikov, D. V. Varentsov, L. M. Shestov, M. E. Rodionova, M. Endres, P.-M. Lang, D. H. H. Hoffmann, and S. Udrea, *Instrum. Exp. Tech.* **59**, 712 (2016).
- ²⁰K. Halbach, *Nucl. Instrum. Methods* **169**, 1 (1980).
- ²¹C. R. Danly, F. E. Merrill, D. Barlow, and F. G. Mariam, *Rev. Sci. Instrum.* **85**, 083305 (2014).
- ²²M. Schanz, M. Endres, K. Löwe, T. Lienig, O. Deppert, P. M. Lang, D. Varentsov, D. H. H. Hoffmann, and O. Gutfleisch, *Rev. Sci. Instrum.* **88**, 125103 (2017).
- ²³K. Makino and M. Berz, *Nucl. Instrum. Methods Phys. Res., Sect. A* **558**, 346 (2006), part of Special Issue: Proceedings of the 8th International Computational Accelerator Physics Conference.
- ²⁴M. Berz, *Nucl. Instrum. Methods Phys. Res., Sect. A* **298**, 473 (1990).
- ²⁵R. Singh, Ph.D. thesis (Technische Universität Darmstadt, 2014).
- ²⁶F. E. Merrill, E. Campos, C. Espinoza, G. Hogan, B. Hollander, J. Lopez, F. G. Mariam, D. Morley, C. L. Morris, M. Murray, A. Saunders, C. Schwartz, and T. N. Thompson, *Rev. Sci. Instrum.* **82**, 103709 (2011).
- ²⁷A. Kalimov, A. Potienko, and H. Wollnik, *IEEE Trans. Appl. Supercond.* **16**, 1282 (2006).
- ²⁸A. Kalimov, H. Leibrock, C. Muehle, and P. Nalimov, *IEEE Trans. Appl. Supercond.* **24**, 1 (2014).
- ²⁹A. Kalimov, H. Leibrock, C. Muehle, P. Nalimov, and P. Rottlander, *IEEE Trans. Appl. Supercond.* **28**, 1 (2018).
- ³⁰H. Enge, *Nucl. Instrum. Methods* **28**, 119 (1964).
- ³¹U. Cobham plc, Opera 3d design software, Wimborne Minster.
- ³²Z. Wang, C. Dujardin, M. S. Freeman, A. E. Gehring, J. F. Hunter, P. Lecoq, W. Liu, C. L. Melcher, C. L. Morris, M. Nikl, G. Pilania, R. Pokharel, D. G. Robertson,

D. J. Rutstrom, S. K. Sjue, A. S. Tremsin, S. A. Watson, B. W. Wiggins, N. M. Winch, and M. Zhuravleva, *IEEE Trans. Nucl. Sci.* **70**, 1244 (2023).

³³C. L. Morris, E. Ables, K. R. Alrick, M. B. Aufderheide, P. D. Barnes, Jr., K. L. Buescher, D. J. Cagliostro, D. A. Clark, D. J. Clark, C. J. Espinoza, E. N. Ferm, R. A. Gallegos, S. D. Gardner, J. J. Gomez, G. A. Greene, A. Hanson, E. P. Hartouni, G. E. Hogan, N. S. P. King, K. Kwiatkowski, R. P. Liljestrand, F. G. Mariam, F. E. Merrill, D. V. Morgan, K. B. Morley, C. T. Mottershead, M. M. Murray, P. D. Pazuchanics, J. E. Pearson, J. S. Sarracino, A. Saunders, J. Scaduto,

A. E. Schach von Wittenau, R. A. Soltz, S. Sterbenz, R. T. Thompson, K. Vixie, M. D. Wilke, D. M. Wright, and J. D. Zumbro, *J. Appl. Phys.* **109**, 104905 (2011).

³⁴C. L. Morris, E. N. Brown, C. Agee, T. Bernert, M. A. M. Bourke, M. W. Burkett, W. T. Buttler, D. D. Byler, C. F. Chen, A. J. Clarke, J. C. Cooley, P. J. Gibbs, S. D. Imhoff, R. Jones, K. Kwiatkowski, F. G. Mariam, F. E. Merrill, M. M. Murray, C. T. Olinger, D. M. Oro, P. Nedrow, A. Saunders, G. Terrones, F. Trouw, D. Tupa, W. Vogan, B. Winkler, Z. Wang, and M. B. Zellner, *Exp. Mech.* **56**, 111 (2016).